Biointerface Research in Applied Chemistry
Open-Access Journal (ISSN: 2069-5837)

Article
Volume 15, Issue 1, 2025, 14
https://doi.org/10.33263/BRIAC151.014

Mass Transfer Study and CFD Simulation in Stirred Tank Reactor with Dual Rushton Turbine Implementing Population Balance Model

Shantanu Chavan [1], Shivanand Teli [1], Sunil Kulkarni [1,*]

[1.] Chemical Engineering Department, Gharda Institute of Technology, Lavel, Khed, India
* Correspondence: suniljayantkulkarni@gmail.com (S.K.)

Scopus Author ID 57209247314
Received: 26.03.2024; Accepted: 20.08.2024; Published: 12.02.2025

Abstract: The performance of the reactor depends on the uniform dispersion and intimate contact between gas and liquid phases. When high conversions of reactants are needed, several tanks in series are used. This investigation determines the volumetric mass transfer coefficient (KLa), bubble size (dB), and specific power consumption in a non-standard container equipped with dual Rushton turbine impellers. The effects of the speed (N) and superficial gas velocity (U_G) on gas hold-up (ϵ_g), volumetric mass transfer coefficient, and upper impeller position are investigated. The position of the bottom Rushton turbine impeller was fixed, while the location of the top impeller was varied two times relative to the bottom impeller. The volumetric mass transfer coefficient (K_{La}) and the Sauter mean bubble diameter (d_B) were plotted against the impeller speed (N) for different superficial gas velocities (U_G). This investigation shows that the position of the top impeller increases the volumetric mass transfer coefficient with significant bubble size reduction. In this research, the gas hold-up is also determined. The gas hold-up and volumetric mass transfer from experimental and prediction methods were agreed upon.

Keywords: gas hold-up; Sauter mean bubble diameter; mass transfer coefficient; computational fluid dynamics; population balance model.

Nomenclature: a=minor axis of a bubble, m; a=Collision frequency; a_i=specific interfacial area, m^2/m^3; b=major axis of a bubble, m ; C1=impeller case 1; C2=impeller case 2; c=impeller clerance ,m; C*=equilibrium dissolved oxygen concentration, mol/m^3 ;C=oxygen concentration, mol/m^3; C_0=initial oxygen concentration, mol/m^3; $C_{L=}$concentration of liquid, mg/l; $C_{D=}$drag coefficient (-); C_{vm} =added/virtual mass coefficients (-); C_μ ,$C_{\varepsilon 1}$, $C_{\varepsilon 2}$, constant (-); σ_K, σ_ε constant (-); d_{Bi}=diameter of bubble class I, m; D_{AB}=diffusivity of oxygen in water, m/s ; d=diameter; d_B=diameter of bubble, m ; d_{bs}=sauter mean bubble diameter, m; E=air flow rate measuring devise ; G=acceleration due to gravity, m/s^2; G=computer; H=total height of reactor, m; H=local height of reactor, m; I=single acting compressor, ; J=circular Sparger ; h/T=height to diameter ratio;$M_{I,L}$ = interfacial forces for liquid, N ; $M_{I,G}$ = interfacial forces for gas, N ; $M_{D,L}$ = drag force, N; $M_{L,L}$ = lift force, N ;$M_{VM,L}$ = virtual mass force, N ;$M_{TD,L}$ = turbulent dispersion force, N ;$M_{W,L}$ = wall lubricating force, N ;n_i = number of the bubbles of size class I; N=impeller speed, rev/min; P=power consumption, w; Q=flow rate of air, m^3/s; ΔP=dynamic pressure, psi; $\Delta P_{O=}$static pressure, psi; $k_{L=}$=local mass transfer coefficient, m/s; k_La=volumetric mass transfer coefficient, 1/s; s=surface renewal rate, 1/s; $t_{p=}$time between the conductivity peaks, s; t=time, s; $U_{G=}$superficial velocity of gas, m/s; U_{slip}=slip velocity, m/s; $V_=$liquid volume, m^3 ; π=Pi ; ω_{ag}=Collision frequency; P_{ag}=Collision efficiency; g (V′)=Breakage frequency; β (V | V′)=Probability density function for breakage; Ω_{br}= Breakage frequency.

Greek symbols: ϵ_G = gas hold up; ϵ_L = liquid hold up ; ρ_L = density of liquid, kg/ m^3; ρ_G = density of gas, kg /m^3; μ_L = viscosity of liquid, Pa · s; μ_W = viscosity of water, Pa · s; $\mu_{L.eff}$ = effective viscosity of a liquid, Pa · s; σ =surface Tension, N/m; v_t = turbulent viscosity, kg/m · s ν_l=kinematic viscosity of liquid, m2/s ; ε=turbulent eddy dissipation rate, m2/s3 ; ψ=aspect ratio (-) λ = kolmogorov length scale, m; τ = torque, N.m .
Subscripts: G=gas phase; K=phase, k=G; g=gas phase; k=L; l=liquid phase; L=liquid phase.
Abbreviations: STR=Stirred tank reactor; CSTR=Continues stirred tank reactor; BSD=Bubble size distribution; PBM=Population balance model; SIMPLE=Semi-Implicit Method for Pressure Linked Equations; MRF=Multiple-reference-frame; EOS=Electro-optical system.

1. Introduction

A continuous stirred tank reactor (CSTR) is used for uniform vessel mixing. In practice, no reactor is ideal. CSTRs are primarily used where continuous agitation is required. CSTRs are used in biological, pharmaceutical, food, and chemical industries. The performance of the reactor depends on the uniform dispersion and intimate contact between gas and liquid phases. When high conversions are needed, several CSTRs in series are used. Mass transfer from the gas phase to the liquid phase is the most crucial factor in the process in gas-liquid reactors.

Aerated CSTR is widely used. However, the main drawback of CSTR is improper mixing due to dead zones. Proper mixing depends on various parameters such as the geometry of the agitators, baffles, and the combinations of the turbine, such as spacing, i.e., clearance between two impellers, etc. If the clearance between the two is minimal, they will act as a single impeller and create a typical flow pattern; while clearance is more, it will act like two CSTRS stacked on each other. To carry out reactions, there should be perfect mixing and effective stirring—the effective mass transfer results in more conversion and quality products. The mass transfer coefficient is crucial in characterizing and designing stirred and non-stirred gas-liquid reactors. The agitator may consist of one or more impellers. Ultimately, reactions between gas-liquid reactants may be observed in some practical cases. The gas hold-up is the volume fraction of gas in the reactor. In a heterogeneous flow regime, because of coalescence and bubble break-up, bubbles can be divided into large or small. The study investigates the effects of the tip velocity of both the agitators with constant agitator diameter on gas hold-up distribution and bubble diameter. Detailed liquid phase flow and local void fraction profiles of the gas phase were presented for different impeller speeds. Currently, CFD and experimentations have mainly investigated the effects of impeller clearance and different impeller speeds on bubble size distribution and mass transfer coefficient. The small bubble size distribution is advantageous in a stirred tank reactor. The smaller bubble size gives more gas back mixing than the large bubble size for the same flow rate and impeller speed. The researchers [1, 2] have investigated average bubble size, interfacial area, air volume fraction, and mass transfer coefficient. Many experts have also studied bubble size distribution for situations where bubbles do not come in contact during their path. Literature also reveals that the bubble size is a strong function of the location [2, 3].

Gas-liquid simulation and experiments were first performed in a single impeller stirred tank reactor at three different impeller speeds of 200, 350, and 700 rpm with different bubble diameters of 0.5mm,1.5mm, and 2.5mm [4]. The multi-impeller gas-liquid stirred tank reactor was also studied experimentally [5]. The investigation determined different hydrodynamic parameters for a rotational speed of 0-8 rps and superficial gas velocity of 5 to 20 mm/s.

Correlations have also been recommended to predict air volume fractional and volumetric mass transfer coefficients. Investigations have also been reported on the multiple impeller-stirred tank reactors to forecast gas-liquid flow patterns, bubble diameter, and different liquid circulation loops in the reactor [6]. The effect of the flooding-loading shift in an aerated, fully baffled stirred tank equipped with dual six-blade Rushton turbines was also studied [7]. Experimental determination of the bubble size distribution was also reported, and it was found that the bubble size depends on the location [2, 3]. Barigou and Greaves found that the bubble size at the tank's walls is lesser than those at the region of the above impeller [8]. Small bubbles are observed in the top impeller region, and within the impeller region, big-sized bubbles are observed. The bubble size mainly depends on the impeller speed at lower gas velocities. However, at higher superficial gas velocity, bubble size is not much varied by impeller speed due to the effect of bubble coalescence [9]. The influence on flow pattern was also reported [10–12]. Mahmoudi and Yianneskis reported that the impeller positions (impeller clearance, i.e., the distance between impellers) affect the flow pattern for keeping all operating parameters constant [13]. Mishra and Joshi maintained maximum clearance between impellers and observed the particular individual flow pattern using the Laser Doppler anemometer method [14]. Similarly, the researchers also observed that impellers create individual flow patterns for maximum clearance, and impellers act like a single impeller for minimum clearance [15].

Various equations for multiphase flow, bubble flow, mass transfer correlations, and population balance models are available in the literature [16-19]. Also, studies regarding multiphase phase flow, its characteristics, the use of a population balance model for gas gas-liquid flow, gas-inducing impeller design, and performance characteristics have been reported by various researchers [20-22]. Multiscale CFD simulations are being explored for different types of contactors and reactors, namely fluidized beds, stirred tanks, and cavitation reactors [23-25]. In the trickle bed, the prediction of pressure drop and catalyst wetting can be made using CFD [26]. Recently, mass transfer studies for stirred tank reactors to improve mass transfer coefficients have been reported. The methods to improve mass transfer include modifications in the flow pattern, blade dimensions, and baffles [27-30]. Kinetic modeling of mineral carbonation for aqueous mineral carbonation has been reported [30]. Jadhav and Barigou used a 3D Eulerian-Lagrangian CFD model to simulate turbulent flow and the mixing of dense particles [31]. Deterministic multiphase models are more challenging, and their computing application is costly [32-35]. A stochastic model can accurately predict 3D two-phase flow [35]. Various investigators found The stochastic optimization model to be accurate and effective [36-38]. Comparisons between deterministic and Stochastic models are also available in the literature [39]. Particle-stabilized dispersion and flocculation modeling have also been done using population balance models [40,41].

The mass transfer coefficient is the mass transfer flux and concentration gradient ratio. The mass transfer coefficient, k, measures the mass transfer that took place per unit area for the available concentration gradient. The mass transfer coefficients can be individual or overall. The mass transfer coefficients are a function of temperature, pressure, physical properties of the fluid, size of the bubbles, the velocity of bubble rise, and gas and liquid velocities. Packed beds with various modifications and stirred tanks with customized designs can be employed effectively for multiphase processes. Intensification of the gas-liquid contactors can be realized to enhance the mass transfer by various modifications to reduce the size. Also, operating costs and resources can be optimized if, in detail, the study and analysis of the mass transfer coefficient is carried out for the contractors.

There is hardly any research on the effect of impeller clearance on the mass transfer coefficient, nor has there been a comparison of different mass transfer models. The impact of impeller clearance on bubble size distribution from CFD simulation using population balance modeling was not reported in the literature. This work for a stirred tank reactor with a dual impeller Rushton turbine determines the mass transfer coefficient from experimental and different mass transfer models. The accurate prediction of bubble size distribution from CFD simulation using the population balance model is made. The influence of impeller clearance on air volume fraction and power consumption is also determined.

2. Objectives

The effect of turbine clearance on bubble size distribution, mass transfer coefficient, gas hold-up, and power consumption in dual impeller Rushton turbine is investigated. The experimental and predicted mass transfer coefficient (KLa) was estimated using different mass transfer models under different operating conditions. The k-epsilon turbulent model was applied with the effect of bubble breaks up and coalescence dual impeller configurations in gas-liquid flow in a stirred tank reactor.

3. Experimental setup

A plane-bottomed cylindrical tank made of transparent acrylic plastic with a diameter of T= 0.3m and H/T=2 was used for the experiment. Four Baffles of 0.1T at 90° to each other were used. Six-bladed Rushton turbines were employed for agitation. There were two impellers placed at two different positions. One of them, at the bottom impeller, was stationary, and for another impeller location it varied relative to the bottom impeller according to the requirement of the experimental study.

Table 1. Operating conditions.

Speed (rpm)	Reynold's number	Gas flow rate (L/min)	Superficial gas velocity m/s	Froude number	Gas flow number
270	44910	2	0.00047	0.20663	0.00740
		4	0.00094	0.20663	0.01481
		6	0.00141	0.20663	0.0222
290	48237	2	0.00047	0.23837	0.0068
		4	0.00094	0.23837	0.0137
		6	0.00141	0.23837	0.02068
310	51563	2	0.00047	0.27239	0.00645
		4	0.00094	0.27239	0.01290
		6	0.00141	0.27239	0.01935

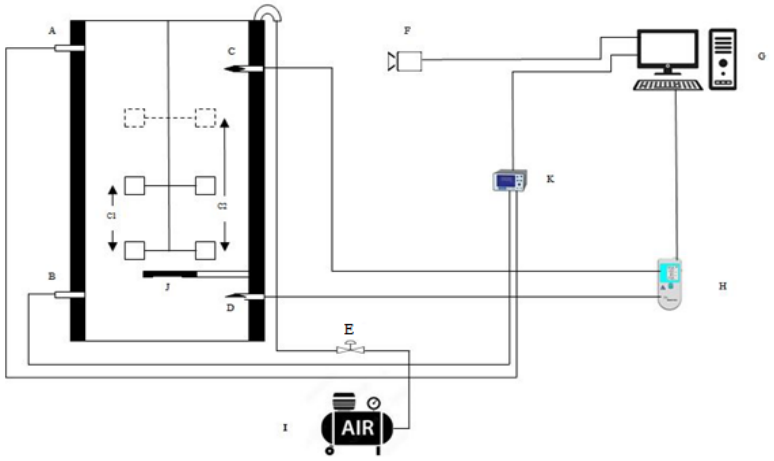

(a)

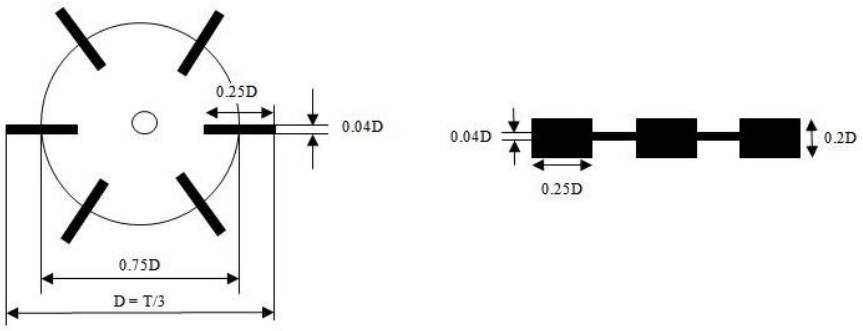

Figure 1. Overall experimental setup **(a)** Experimental Schematic Diagram; **(b)** Impeller Geometry 6 Blade Rushton Turbine.

Two cases were considered: Case 1(C1): upper impeller location was kept h/T= 0.88, and Case 2(C2): upper impeller location was kept h/T=1.21. Sparger was used to force the gas (compressed air). The diameter of the sparger was 0.15 m, and it had 32 holes on it. The diameter of each hole was 2 mm. Here, the dispersed phase is air, and the continuous phase is water. Experiments were performed for different superficial gas velocities and different impeller rotation speeds. The experimental and simulation operating conditions for the work are shown in Table 1.

3.1. Measuring systems.

3.1.1. Gas hold-up measurement.

Pressure measurement is required to measure air volume fraction. The air volume fraction is determined by measuring pressure difference using the pressure sensors located at the ’s top and bottom portions. The A and B are pressure-measuring devices in the overall experimental setup, as shown in Figure 1. The pressure monitoring system was used to display pressure measurements from pressure sensors. The K is a pressure measuring with a data acquisition meter, as shown in figure1. The computer acquires pressure measurement data with a frequency of 60 Hz. In a sense, have one reading per second. It has a 0-30 PSI range and an accuracy of 0.1%.

Two pressure sensors were placed at the bottom and top sides to measure pressure drop. The bottom one was located at a distance of H/T=0.13, and the top side was at a distance of H/T=1.6. A stainless steel tube capsule protects the pressure sensors. The formula determined the gas hold-up:

$$\epsilon_g = \left(1 - \frac{\Delta P}{\Delta P_0}\right) \quad (1)$$

Where ϵ_g= gas hold-up

ΔP= dynamic pressure drop at $U_G > 0$

ΔP_0 = static pressure drop at $U_G = 0$

U_G = superficial gas velocity

3.1.2. Dissolved oxygen measurement.

D.O**.** measurement is required to calculate the mass transfer coefficient. The dissolved oxygen probes were used to determine dissolved oxygen concentration in water. Here, in the present work, two dissolved oxygen probes were used. The C and D are dissolved oxygen sensors located in the top and bottom portion of the reactor, and H is a dissolved oxygen meter

with a data acquisition meter, as shown in figure 1. The computer acquires dissolved oxygen readings with a frequency of 10Hz. The range of sensors is 0 to 19.9 ppm, and it can measure between temperature ranges of 0°C to 50°C. Before Experimenting, the dissolved oxygen already present in tap water is removed by sparging inert gas like nitrogen. After the dissolved oxygen concentration became 0 ppm, experiments were carried out. The dissolved oxygen concentration was measured at 30°C throughout the experiments. Probes are located at two different locations; one is on the bottom side, and one is on the top side, as shown in figure1. The graphical technique is used to calculate the volumetric mass transfer coefficient (K_La)(figure 2). The following equation can give the accumulation of oxygen in the water:

$$\frac{dC}{dt} = K_La\,(C^* - C) \quad (2)$$

Where C* is the equilibrium concentration of oxygen and $\frac{dC}{dt}$ is the change in concentration concerning time. After integrating and putting boundary conditions, the volumetric mass transfer coefficient (K_La) is calculated by:

$$\ln\left(\frac{C^*-C}{C^*-C_0}\right) = K_La \times t. \quad (3)$$

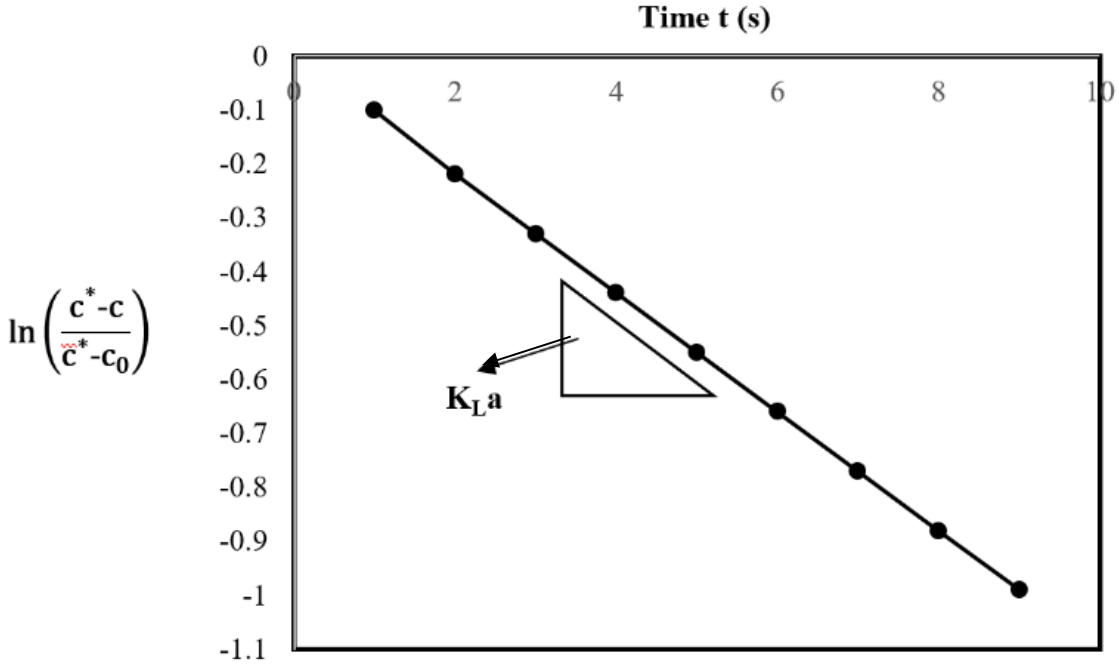

Figure 2. Sample graph of volumetric mass transfer coefficient.

3.1.3. Power measurement.

Power requirement for two different configurations of agitator Case 1 and Case 2 is the main parameter for the stirred tank reactor. The power requirement was calculated by measuring torque and speed of rotation. The torque was directly calculated by the torque meter (Remi Elektrotechnik Limited, the model RQ-40 plus). It consists of a motor, meter, and LCD for reading torque values. The whole assembly is fitted within a single body. It has a stirring capacity of 40 liters with a range of 0.01 to 0.6 Nm.

The power required can be measured by a formula:

$$P = 2\pi N\,\tau \quad (4)$$

Where:

P= Power required (watt)

N= No of rotation (rps)

τ = torque (N.m)

3.1.4 Bubble size measurement

The image processing method was used with a high-definition camera (Canon EOS 1500D DSLR) to measure bubble sizes. F is the Camera located near the top position of the reactor, as shown in Figure 1. The rectangular vessel was used to avoid optical reflections from the curvy wall. The stirred tank reactor was located in it, containing water for a volume of 36 L. The bubbles at the closer wall of the stirred tank reactor were considered representative of those inside the reactor. The bubble size was calculated with the help of a Web Plot digitizer. 100 to 150 bubbles were selected for a given hydrodynamic condition, and their diameters were estimated. The local bubble diameter is determined using the following relationship:

$$d_{eq} = 2\sqrt[3]{a^2 b} \quad (5)$$

$$\psi = \frac{b}{a} \quad (6)$$

From equations 5 and 6, we get:

$$d_{eq} = 2a\psi^{1/3} \quad (7)$$

Where a and b are the major and minor axis of the bubbles. This method was used to calculate the average bubble size. The local values of bubble size are calculated by following equation 8**.**

$$d_B = \frac{\sum_i^n ni\ dBi^3}{\sum_i^n ni\ dBi^2} \quad (8)$$

Where dB_i is the individual diameter of the bubble and n_i is the number of bubbles.

4. Models

4.1. CFD models.

4.1.1. Governing equation.

There are two different methods for gas-liquid flow simulations. **(a)** Eulerian - Lagrangian models **(b)** Eulerian - Eulerian models. The Eulerian – Lagrangian approach considers the trajectory of each 'phase's motion and solves the 'fluid's dynamics at a microscopic length scale(smaller than the bubble diameter). Eulerian - Eulerian approach treats the fluid and fluid phases as interpenetrating continua and studies their dynamics employing averaged equations of motion. The concept of void volume and volume fraction is used to explain the area occupied by individual phases. The gas-liquid volume fractions, along with mass and momentum conservation equations, can be written for the system. The volume fraction(α) needs to satisfy equation 9.

$$\sum_{k=1}^{n} \alpha_k = 1 \quad (9)$$

Where n is the total number of phases, the instantaneous local balance is averaged for each phase while writing the conservation equations. Only two phases are needed to describe gas-liquid flows, n = 2. There are two types of flow: gas-dispersed and liquid dispersed.

CFD simulation of the stirred tank reactor has been carried out using a standard k-epsilon turbulent model. The following governing equations are reported in the literature

4.1.1.1. Continuity equation.

$$\frac{\partial}{\partial t}(\rho_k \epsilon_k) + \nabla(\rho_k \epsilon_k u_k) = 0 \quad (10)$$

4.1.1.2. Momentum transfer equation

$$\frac{\partial}{\partial t}(\rho_k \epsilon_k u_k) + \nabla(\rho_k \epsilon_k u_k u_k) = -\nabla(\epsilon_k \tau_k) - \epsilon_k \nabla P + \epsilon_k \rho_k g + M_{I,k} \quad (11)$$

The terms on the right-hand side of the equation (11) represent the stress, the pressure gradient, gravity, and the collective-averaged momentum interchange between the phases, respectively. The stress term of phase k is described:

$$\tau_k = -\mu_{eff,k} (\nabla u_k + (\nabla u_k)^T - \frac{2}{3} I(\nabla u_k) \quad (12)$$

Where $\mu_{eff,k}$ is effective viscosity; the effective viscosity of the liquid phase is composed of three contributors: molecular viscosity, turbulent viscosity, and an additional term due to bubble-induced turbulence.

$$\mu_{eff,L} = \mu_L + \mu_{T,L} + \mu_{BI,L} \quad (13)$$

The calculation of effective gas viscosity is based on the effective liquid viscosity as follows:

$$\mu_{eff,G} = \frac{\rho G}{\rho L} \mu_{eff,L} \quad (14)$$

Turbulence induced by the movements of bubbles can be calculated by the model proposed by [16]:

$$\mu_{BI,L} = \rho_L C_{\mu,BI} \epsilon_G d_B |\mu_G - \mu_L| \quad (15)$$

With a model constant $C_{\mu,BI} = 0.6$

To close the system of equations, turbulent eddy viscosity has been formulated using k and ε:

$$\mu_{T,L} = \rho_L C_\mu \frac{k^2}{\varepsilon} \quad (16)$$

The momentum exchange energy in equation (11) The interfacial force term MI,k represents the interaction forces between the gas and liquid phase. The formulation of these forces is given in the following section. Therefore, the total interfacial force acting between gas-liquid phases can be formulated as:

$$M_{I,L} = -M_{I,G} = M_{D,L} + M_{L,L} + M_{VM,L} + M_{TD,L} + M_{W,L} \quad (17)$$

4.1.2. Turbulent Equations

The turbulent kinetic energy (k) and turbulent energy dissipation (ε) are considered respectively based on the following governing equation:

$$\frac{\partial}{\partial t}(\rho_k \epsilon_L k) + \nabla(\rho_L \epsilon_L u_L k) = -\nabla(\epsilon_L \frac{\mu_{eff,L}}{\sigma_k} \nabla k) - \epsilon_L (G - \rho_L \varepsilon) \quad (18)$$

The rate of dissipation of turbulent kinetic energy is calculated from its governing equations:

$$\frac{\partial}{\partial t}(\rho_L \epsilon_L \varepsilon) + \nabla(\rho_L \epsilon_L u_L \varepsilon) = -\nabla\left(\epsilon_L \frac{\mu_{L,eff}}{\sigma_\varepsilon} \nabla \varepsilon\right) + \epsilon_L \frac{\varepsilon}{k} (C_{\varepsilon 1} G - C_{\varepsilon 2 \rho_L} \varepsilon) \quad (19)$$

In the Reynolds stress model, individual Reynolds stresses u_i' 'uj' are computed via a differential transport equation. The exact transport equations for the transport of Reynolds stresses $\rho u_i' u_j'$ are given by:

$$\frac{\partial}{\partial}(\rho_L \overline{u_i' u_j'}) + \frac{\partial}{\partial x_k}(\rho_L u_K \overline{u_i' u_j'}) = P_{ij} + \emptyset_{ij} + \frac{\partial}{\partial x_k}\left(\left(\mu + \frac{2}{3} C_s \rho \frac{k^2}{\varepsilon}\right) \frac{\partial \overline{u_i' u_j'}}{\partial x_k}\right) - \frac{2}{3} \delta_{ij} \rho_L \varepsilon \quad (20)$$

Where $\emptyset_{ij}$ is the pressure-strain correlation, and P is the exact production term given by:

$$p = -\rho(\overline{u_i' u_j'}(\nabla u)^T + (\nabla u)\overline{u_i' u_j'}) \quad (21)$$

As the turbulence dissipation appears in the individual stress equations, an equation for ε is computed with the model transport equation:

$$\frac{\partial}{\partial t}(\rho_L \epsilon_L \varepsilon) + \frac{\partial}{\partial xi}(\rho_L \epsilon_L ui\, \varepsilon) = \frac{\partial}{\partial xj}\left(\epsilon_L \left(\mu + \frac{\mu_t}{\sigma_\varepsilon}\right)\frac{\partial \varepsilon}{\partial xj}\right) + \epsilon_L C_{\varepsilon 1} \rho_L \left(\overline{u_i' u_j'}\frac{\partial ui}{\partial x_k}\right)\frac{\varepsilon}{k} - \epsilon_L C_{\varepsilon 2} \rho_L \frac{\varepsilon^2}{k} \quad (22)$$

The standard model parameters have been considered in present simulations, such as C_μ = 0.09, $C_{\varepsilon 1}$=1.44, $C_{\varepsilon 2}$=1.92, σ_k =1.0 and σ_ε =1.3. The term G in the above equation is the production of turbulent kinetic energy and is described by:

$$G = \tau_L : \nabla u_L \quad (23)$$

These equations are solved using a finite volume approach.

4.2. Population balance model.

The type of flow encountered in a stirred tank reactor is polydispersed multiphase flow. A general form of the population balance equation is:

$$\frac{\partial n_i}{\partial t} + \nabla.(u_G n_i) = B_B + B_C - D_B - D_C \quad (24)$$

Where u_G is the gas velocity, represents the number densities of size group i, and terms on the right-hand side B_B, B_C, D_B, and D_C are, respectively, the "birth" and "death" due to breaking up and coalescence of bubbles. The bubble number density n_i is related to the gas volume fraction ϵ_G by:

$$\epsilon_G f_i = n_i V_i \quad (25)$$

Where represents the volume fraction of bubbles of group i and V_i is the corresponding volume of a bubble of group i. The rate of birth of group i bubble due to the breakage of the larger bubble is given below equation (26):

$$B_B = \sum_{j=i+1}^{N} g(V_j : V_i) n_j \quad (26)$$

The rate of birth of i group by coalescence of j and k group bubbles is given by equation (27).

$$B_c = \frac{1}{2}\sum_{j=1}^{i}\sum_{k=1}^{i} Q_{jk} n_j n_K \quad (27)$$

The rate of death of i group bubble because of breakage into smaller bubbles is given by equation (28).

$$D_B = g_i n_i \quad (28)$$

The birth rate of i group by coalescence of j and k group bubbles is given below equation (29).

$$D_C = n_i \sum_{j=1}^{N} Q_{ij}\, n_j \quad (29)$$

4.2.1. Bubble break-up model.

The product of the frequency of breakage and probability density function for the particles that are breaking out of total volume can be represented in the bubble breakage model. The bubble breakage model is applied to estimate the number of bubbles formed during the breakage. It can also be used for the size of the bubbles and the rate of formation.

$$\int_0^{V'} \beta\,(V|V')dV = 1 \quad (30)$$

(2) The addition of the masses of the daughter particle after breakage must be equal to the original particle mass:

$$p \int_0^{V'} m\,(V)\beta(V|V')dV = m(V') \quad (31)$$

Moreover, (3) the numbers of daughter particles formed must be correctly represented; that is, for binary breakage, β is symmetric about $V|V' = 0.5$. The parent particle volume is denoted by V', and the daughter particle volume is denoted by V.

4.2.2. Bubble coalescence model.

The coalescence model mechanism is based on the collision between two particles, ultimately resulting in coalescence. The various studies proposed different criteria for the coalescence mechanism. In our study, we have considered three different coalescence models. A detailed explanation of the models is presented in the following section.

4.3. Mass transfer models.

By definition, interfacial area a_{ij} for gas-liquid flow through a stirred tank reactor can be determined through the relationship. Interfacial area $a_{ij,}$ along with the Sauter mean bubble diameter, are important parameters that link the interaction between the liquid and gas phases:

$$a_{ij} = \frac{6\epsilon_G}{d_s} \quad (32)$$

Where ϵ_G overall gas hold is determined from pressure measuring techniques and d_s Sauter mean bubble diameter:

$$d_s = \frac{1}{\sum_i \frac{f_i}{d_i}} \quad (33)$$

Where d_S is the Sauter mean bubble diameter. The local Sauter mean bubble diameter can be deduced based on the calculated values of the scalar fraction fi and discrete bubble sizes di. The overall volumetric mass transfer coefficient (k_La) is measured from the product of the overall mass transfer coefficient (k_L) and interfacial area (a_{ij}). Several models are available in the literature for calculating the local mass transfer coefficient (k_L), but the commonly used model is based on penetration theory and surface renewal model. According to Higbie's penetration theory, the liquid phase mass transfer coefficient of a bubble with a movable surface is represented by:

$$k_L = 2\sqrt{\frac{D_l}{\pi\, t_e}} \quad (34)$$

Where D_l diffusivity of oxygen in water and t_e is contact time so calculated from 'Kolmogorov's length scale of isotropic turbulence ($t_e = \sqrt{\nu_l}/\varepsilon_1$); where ν_l kinematic viscosity of liquid and ε_l turbulent eddy dissipation rate. Equation (34) becomes:

$$k_L^{penetration} = \frac{2}{\sqrt{\pi}} D_l^{0.5} \left(\frac{\varepsilon_l}{\nu_l}\right)^{0.25} \quad (35)$$

This model is denoted as $k_L^{penetration}$ .The mass transfer coefficient (k_L) suggested by Danckwert [18] is given by the equation $k_L = \sqrt{D_l s}$ where **s** is a fraction of the surface renewal rate. The D_l is the diffusivity of oxygen in the water. The k_L is related to an average bubble interface surface renewal rate between eddies with variable contact time. The mass transfer coefficient (k_L) is suggested by many researchers based upon a theory of isotropic turbulence is given by:

$$k_L^{eddy\ cell} = K\ D_l^{0.5} \left(\frac{\varepsilon_l}{\upsilon_l}\right)^{0.25} \quad (36)$$

This model is denoted as $k_L^{eddy\ cell}$ and generally referred to as the eddy cell model. Where D_l is the diffusivity of oxygen in water,υ_l is the dynamic viscosity of the liquid, ε_l is turbulent eddy dissipation rate and k = 0.4 model constants. The bubble has a mobile interface, and the gross mean flow of the liquid relative to the bubble (slip velocity) controls the renewal of the liquid phase and contact time can be expressed in terms of average bubble size and average slip velocity as:

$$k_L^{\text{slip velocity}} = \frac{2}{\sqrt{\pi}}\sqrt{\frac{D_l U_{slip}}{d_B}} \quad (37)$$

Where U_{slip} is the slip velocity of two phases (gas and liquid), which can be determined by a difference in gas-liquid velocity from CFD simulation modified the equation of k_L based on bubble rigidity and is denoted as k_L^{rigid}, and this is obtained from the equation proposed by [19] based on laminar boundary value theory as:

$$k_L^{rigid} = C\left(\frac{U_{slip}}{d_B}\right)^{0.5} D_l^{2/3}\nu_l^{-1/6} \quad (38)$$

Where C is constant taken equals 0.6 and ν_l is the kinematic viscosity of water. The volumetric mass transfer coefficient (k_La) is determined using the mass transfer coefficient of different models and specific interfacial area determined from equation (53). The graphical method determines the experimental volumetric mass transfer coefficient, as described in 2.1.2. Section. The experimental volumetric mass transfer coefficient for different plate configurations I and II are compared with different mass transfer models.

4.4. Numerical solutions.

Commercial computational fluid dynamics ANSYS fluent software was used to perform CFD simulations. The high-resolution discretization scheme was adapted to discretize the partial differential equation associated with it. Fluent uses the cell-centered finite volume method to solve discretized partial differential equations. The multiple reference frames (MRF) approach was used. For solving using MRF, the stirred-tank geometry is divided into two parts. One is a rotating impeller domain, and another is a stationary tank domain. The continuity equation and momentum equations are solved in the rotating framework for impellers, and other equations are solved in the stationary part of the tank. MRF passes the information from the rotating domain to the stationary. The simulation is carried out using a transient approach. Pressure velocity coupling was done using the SIMPLE algorithm. The boundary conditions and gas inlet were defined at the ring sparger to introduce gas below the bottom impeller. For simulation, water and air phases are defined as continuous and dispersed phases, respectively.

4.4.1. Initial and boundary conditions.

The air volume fraction is zero in the tank, and the unsteady state calculation started by assuming that the liquid and gas phases were stagnant. The air volume fraction at the inlet boundary of the computational domain was unity, while the inlet superficial gas velocities were set to be 0.00047, 0.00094, and 0.00141 m/s. The following equation for the size of bubbles generated at the sparger is reported in the literature [2]. The sparger has 32 openings; each hole becomes 3 mm in diameter.

$$d_b = \left(\frac{6\,\sigma\,d_s}{g\,(\rho_l-\rho_g)}\right)^{1/3} \quad (39)$$

The calculated diameter of d_b = 5.1 mm; thus, the Bin 6 fraction bubble group is set to be unity for the inlet condition. Table 2 depicts bin size distribution.

Table 2. Bin sizes distribution.

Bin Number	Bin Size (m)	Bin Number	Bin Size (m)
Bin-0	0.016	Bin-12	0.001
Bin-1	0.012	Bin-13	0.0008
Bin-2	0.01	Bin-14	0.00063

Bin Number	Bin Size (m)	Bin Number	Bin Size (m)
Bin-3	0.008	Bin-15	0.0005
Bin-4	0.0064	Bin-16	0.0004
Bin-5	0.005	Bin-17	0.00031
Bin-6	**0.004**	Bin-18	0.00025
Bin-7	0.0032	Bin-19	0.0002
Bin-8	0.0025	Bin-20	0.00015
Bin-9	0.002	Bin-21	0.00012
Bin-10	0.0016	Bin-22	0.0001
Bin-11	0.0012		

4.5. Grid independency study.

The grid independence study is essential for the optimum elements (figure 3). The accuracy increases as the element size decreases, but the element number increases as we reduce the element size. There is such a point that a further decrease in the size of the element does not affect the solution's accuracy. That size is considered optimum so that the computation time is lowered without compromising the accuracy. Here, four grids were generated(Table 3).

Table 3. Mesh information with different element sizes and element numbers.

Grids	C1 CASE		C2 CASE	
	Element Size (mm)	Element Number	Element Size (mm)	Element Number
1	1.5-3	1625004	1.5 – 3.0	1624938
2	0.4-3.2	1456740	0.4-3.2	1458898
3	2.0-4.0	703612	2.0-4.0	703615
4	0.8-6.4	275587	0.8-6.4	275679

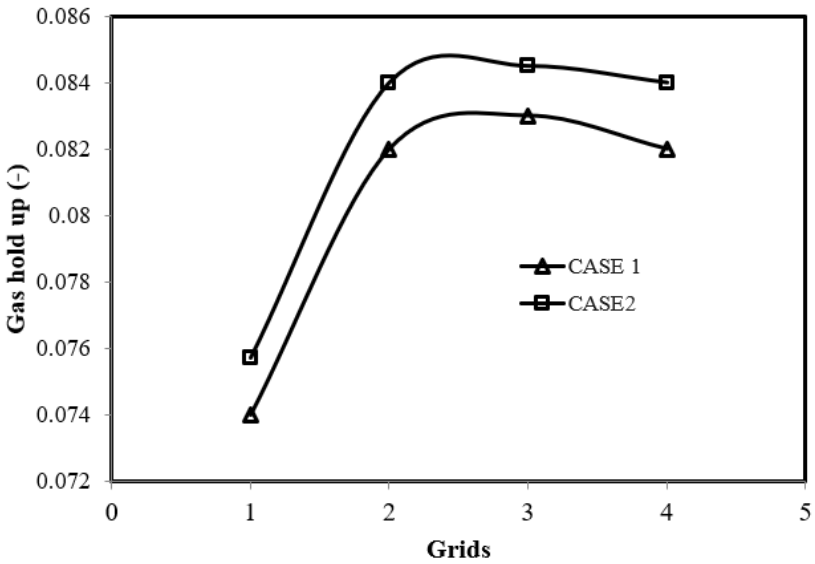

Figure 3. Effect of grids on gas hold-up, (N =290 rpm, U_G = 0.00094 m/s) for impeller configuration C1 & C2 case for the effect of grids on gas hold-up

For fluent meshing, the cut cell assembly method has been adapted. Finer mesh is generated near the impeller to predict velocity variation near the impeller correctly. The average gas hold-up is calculated in a stirred tank reactor at impeller speed 290 rpm and superficial gas velocity 0.00094 m/s, after plotting the graph of gas hold-up Vs. Grids, it is seen that the gas hold-up values of grid 2 (703612), grid 3 (1456740), and grid 4 (1625004) are nearly the same. Hence, for further simulations, grid 2(703612) is adapted.

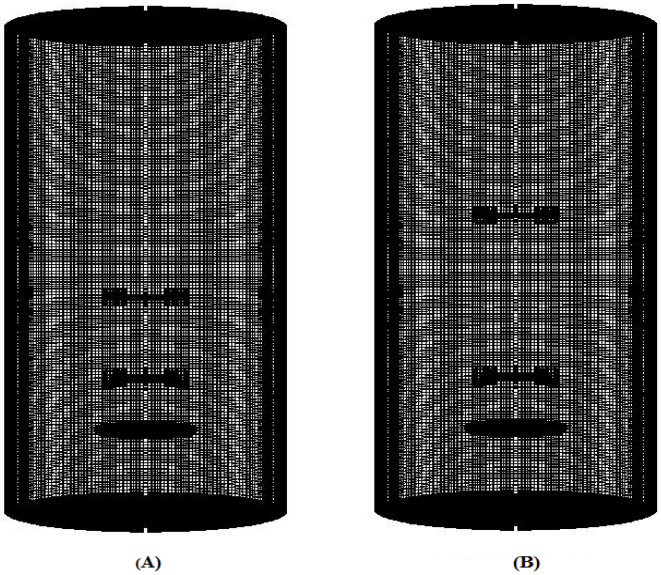

Figure 4. Computational grid and solution domain for **(A)** C1 case; **(B)** C2 case.

4.6 Bin sensitivity study.

A study of the effect of bin sizes and numbers was done. A Bin sensitivity study is important for predicting suitable bin numbers. For simulating this, the operating parameters were kept at 290 rpm and superficial gas velocity U_G = 0.00094 m/s. Keeping the minimum and maximum value of bubble diameter size constant, the bin number was varied. Four different bin numbers were selected: 7, 9, 12, and 23. The minimum bubble size was kept at 0.1mm, while the maximum bubble size was kept at 16.32mm. This minimum and maximum bubble size was predicted using the experimental data, and a uniform distribution of bins was done. Fluent is used for this population balance model in ANSYS. Different bins are discretized as:

$$\frac{d_{i+1}}{d_i} = 2^q \quad (40)$$

Where q = 3.66, 2.75, 2, 1 for bin 7, 9, 12, 23 respectively.

The above equation 60 was reported in the literature to discretize different bin sizes [20]. Figure 4 depicts the computational grid and solution domain for (A) C1 case and (B) C2 case.

For the bin sensitivity study, three locations were selected above the bottom impeller, between two impellers, and above the upper impeller having a total height to corresponding height ratio as (a) H/h = 3.4286, (b) H/h = 2.353, and (c) H/h = 1.348 respectively**.** The bubble size vs. percentage graph was plotted from the 'simulation's resulting data. From the graph, it can be observed that the experimental and bin 23 data match. Hence bin 23 was selected for further simulations. For the prediction of bubble size distribution, the experimental data on bubble size was calculated using WebPlot Digitizer software to plot bubbles in an image. The simulations were carried out for the flow conditions of U_G = 0.00094 m/s. Experimental measurements of BSD were provided at the same axial locations as discussed above. Simulations have been performed using the validated and developed CFD model. Bin sensitivity analysis has been performed to predict the BSD accurately. Four bins, 7, 9, 12, and 23, have been selected, and the predictions were drawn in Figure 5. Figure 5 (a) shows the prediction of BSD at H/h = 3.4286. From this Figure, 7-bins, 9-bins, and 12-bins over-predict the BSD, and 23-bins give somewhat realistic results. The prediction of BSD at H/h = 2.353

and 1.348 is plotted in Figures 5 (b) and (c). In these plots, the 7-bins, 9-bins, and 12-bins still over-predict the BSD, but the 23-bins match experimental data.

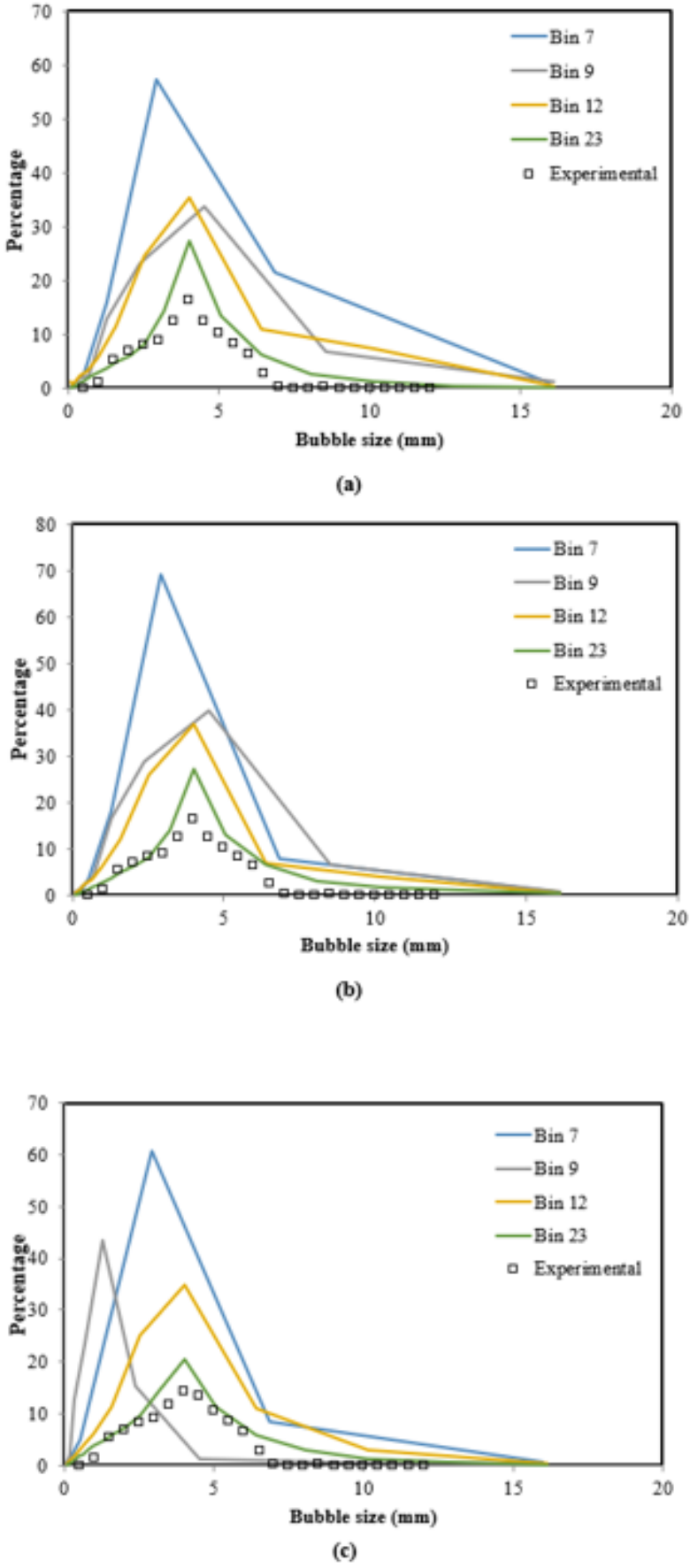

Figure 5. Bin sensitivity study, Bin sensitivity study for bubble size distribution for different locations (a) H/h = 3.4286, (b) H/h = 2.353, & (c) H/h =1.348 for U_G = 0.00094 m/s & impeller speed 290 rpm

5. Results and Discussion

The regimes are classified in terms of dimensionless numbers, namely the gas flow number FlG, $Fl_G = \frac{Q^3}{ND}$ and Froude number Fr, $F_r = \frac{N^2D}{g}$ where Q, N, D, the sparger, the impeller speed, and g are the gas flow rate from the sparger, the impeller speed, the impeller diameter, and the acceleration due to gravity. There is an increase in the Froude number and a decrease in the flow number with impeller speed. The flow regimes depend on shape and size, spacing, design, speed and types of impellers, and gas flow rate in CSTR [21].

5.1. Effect of impeller configuration on gas hold-up (єG).

The gas hold-up in a stirred tank reactor is an extensive function of the distance between two or more impellers and internals of reactors like baffles type of impellers used, etc. Here, the CFD model was used to study gas hold-up for different operating conditions. The impeller speed (N) varied from 270 rpm to 310 rpm, and superficial gas velocity(UG) varied from 0.00047 m/s to 0.00141 m/s. The rise velocity of the bubble is a function of equivalent diameter, and it is directly proportional to it. It has been observed that the overall gas hold-up value increases for both configurations with increasing gas flow rate and rotation speed. This is because when gas is introduced through the sparger, it rises through the center and hits the impeller. As impeller speed increases, bubble break-up increases, the equivalent diameter decreases, so rise velocity decreases, and gas hold-up increases. Similarly, when impeller clearance is less, the gas hold-up is less, while increasing clearance increases gas hold-up; when clearance is less, both impellers form a common flow pattern and act as a single impeller. When impeller clearance is higher, they form individual flow patterns. For the C1 case, introduced gas hits the impeller; there is only a single breaking action on bubbles, while for the C2 case, there is a double breaking action on bubbles, further reducing bubble size. Air volume fractions are indicated for different impeller speeds for both cases in Figure 6. For the C2 case, a circulating vortex is formed a circulating vortex is formed, as shown in water velocity vectors in Figure 7, which causes gas bubbles to get trapped between them. Figure 6 shows the air volume fraction for both configurations at N = 290 rpm and U_G = 0.00094 m/s. The water velocity vector at two impeller locations for different impeller speeds for fixed superficial gas velocity is depicted in Figure 8. Table 4 shows experimental and overall gas hold-up for dual impeller configuration.

Table 4. Experimental and CFD simulation of overall gas hold-up for dual impeller configuration.

Gas Flow rate (LPM)	Impeller Speed (rpm)	Gas hold-up ($є_G$)			
		C1 case		C2 case	
		Experimental	CFD simulation	Experimental	CFD simulation
2	270	0.00265	0.00243	0.00324	0.00274
	290	0.00278	0.00251	0.00327	0.00318
	310	0.00285	0.00263	0.00349	0.00320
4	270	0.00284	0.00270	0.00350	0.00338
	290	0.00288	0.00275	0.00364	0.00339
	310	0.00291	0.00281	0.00372	0.00376
6	270	0.00292	0.00280	0.00372	0.00409
	290	0.00289	0.00342	0.00376	0.00448
	310	0.00307	0.00356	0.00381	0.00459

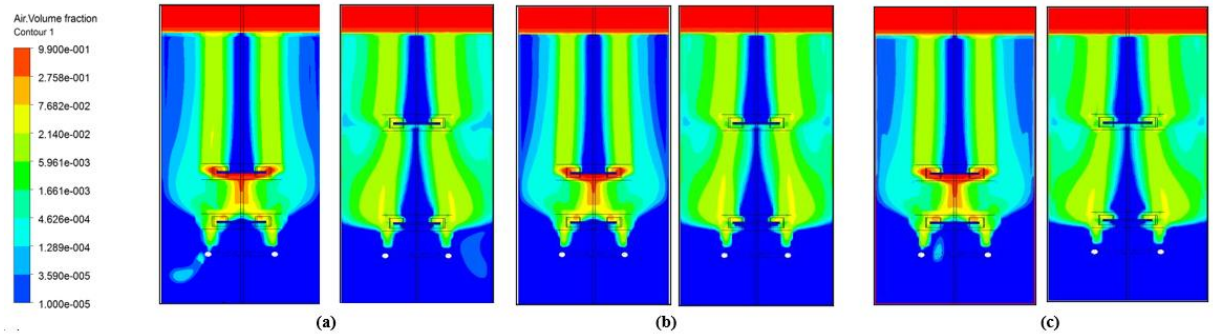

Figure 6. Air volume fraction for C1 and C2 cases at different speed **(a)** 270 rpm; **(b)** 290 rpm; **(c)** 310 rpm for U_G = 0.00094 m/s.

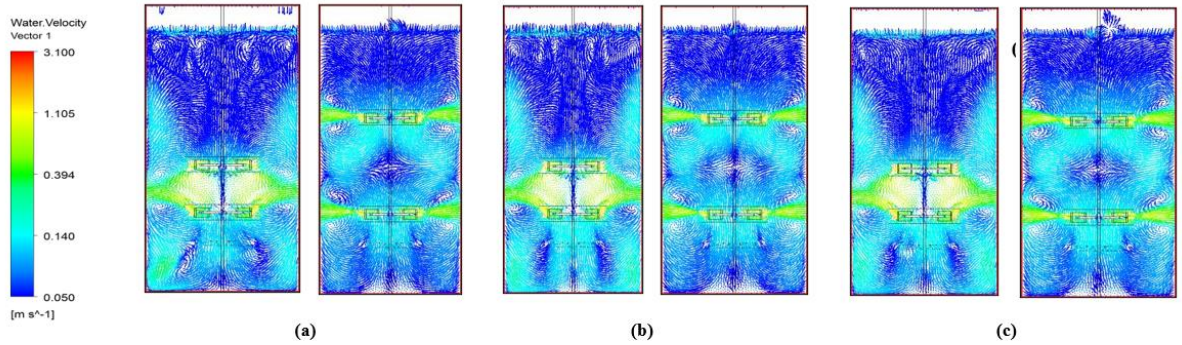

Figure 7. Water velocity vector for C1 and C2 case at different speed **(a)** 270 rpm; **(b)** 290 rpm; **(c)** 310 rpm for U_G = 0.00094 m/s.

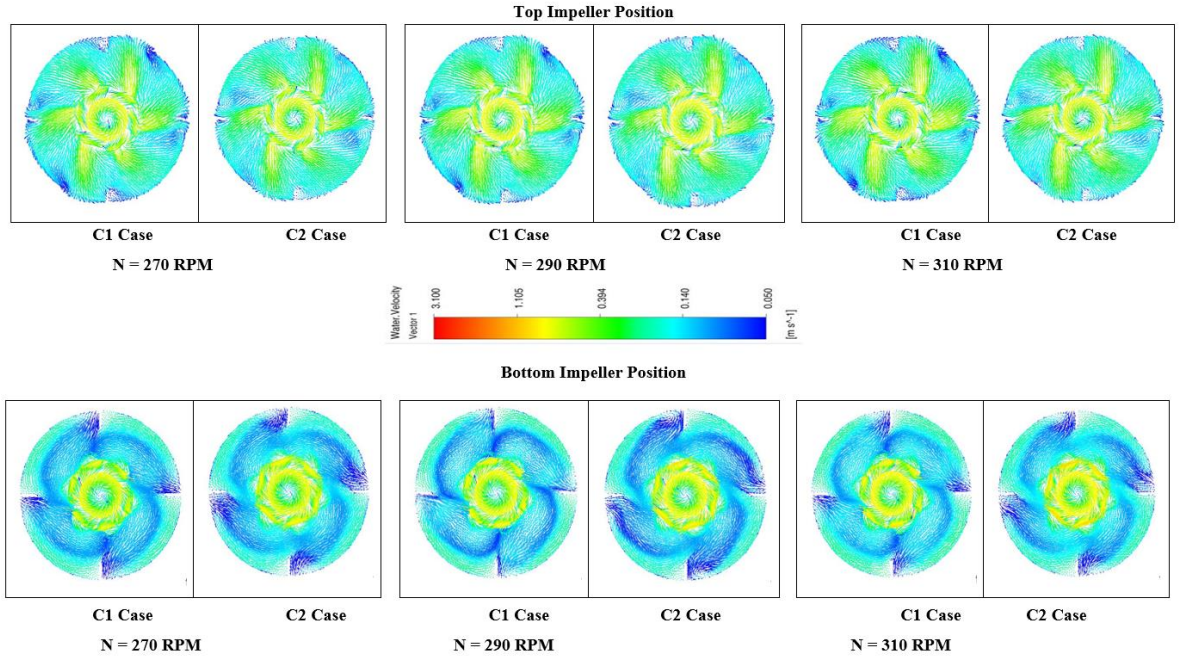

Figure 8. Water velocity vector at two impeller locations for different impeller speed for superficial gas velocity UG= 0.00094 m/s.

5.2 Effect of impeller configuration on bubble size distribution

The bubble sizes are measured at the top portion of the vessel h/T=1.2 from h/T=1.6 and above the impellers. The lower impeller position was kept constant relative to the lower impeller; the position of the upper impeller changed two times for the C1 case, which was 100mm, while for the C2 case, it was 200mm. The snapshots of the bubble size distribution for

C1 cases and C2 cases were captured for different operating conditions. After capturing photos, they are plotted using Web Plot Digitizer, and bubble size is calculated. Sauter mean diameter is calculated as discussed in section 2.1.4. From the calculated size C1, a larger number of bubbles was observed. The U_G = 0.00047 m/s and different rotation speeds 270,290 and 310 rpm for the C1 case; the Sauter mean bubble diameter is 4.75 mm, 4.15 mm, and 4.01 mm. Similarly, for the same superficial gas velocity and rotation speeds of 270, 290, and 310 rpm for the C2 case, Sauter's mean bubble diameter is 4.37 mm, 4.008 mm, and 3.95 mm.

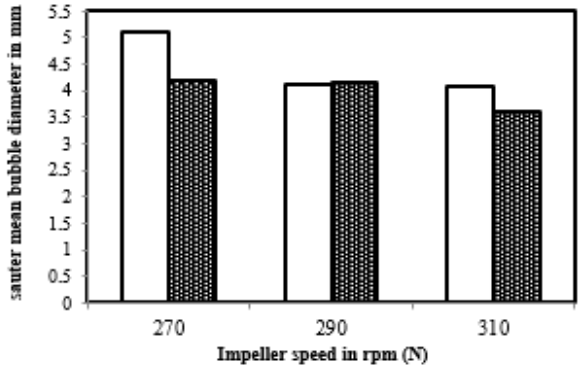

(a) U_G = 0.00047 m/s

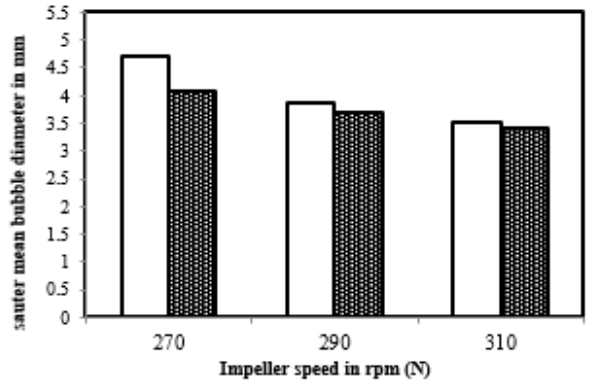

(b) U_G = 0.00094 m/s

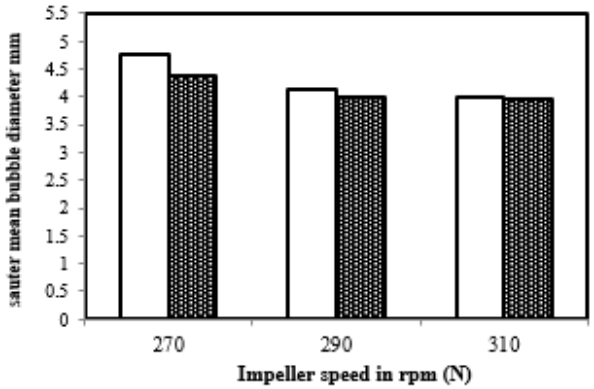

(c) U_G = 0.000141 m/s

Figure 9. Sauter mean bubble diameter Vs. Impeller speed at different superficial gas velocities for the case of C1 (□)& C2 (▩).

It is seen that for similar operating conditions, the bubble size for the C2 case is less than that for the C1 case, as shown in Figure 9.This is mainly because when sparged gas hits the bottom impeller, it disperses gas away in the radial direction, and hence, the gas does not

reach the upper impeller in the C1 case. Above the impeller, as gas moves upward toward the top of the reactor, bubbles coalesce, and hence bubble size increases. However, for the C2 case, the impeller clearance is greater after hitting the bottom; impeller bubbles break into smaller sizes and form several bubbles. After that, it again comes into the vicinity of the shaft and hits the upper impeller to form smaller bubbles. As the rotation speed increases, the tip velocity of the impeller increases due to the high tip velocity bubble break-up increases as shearing increases. To increase the rotation speed of the impeller, there is a decrease in bubble size, as shown in Figures 9 a, b, c. Figure 10 shows the bubble diameter along the axial position for C1 and C2 case impeller configurations for different impeller speeds.

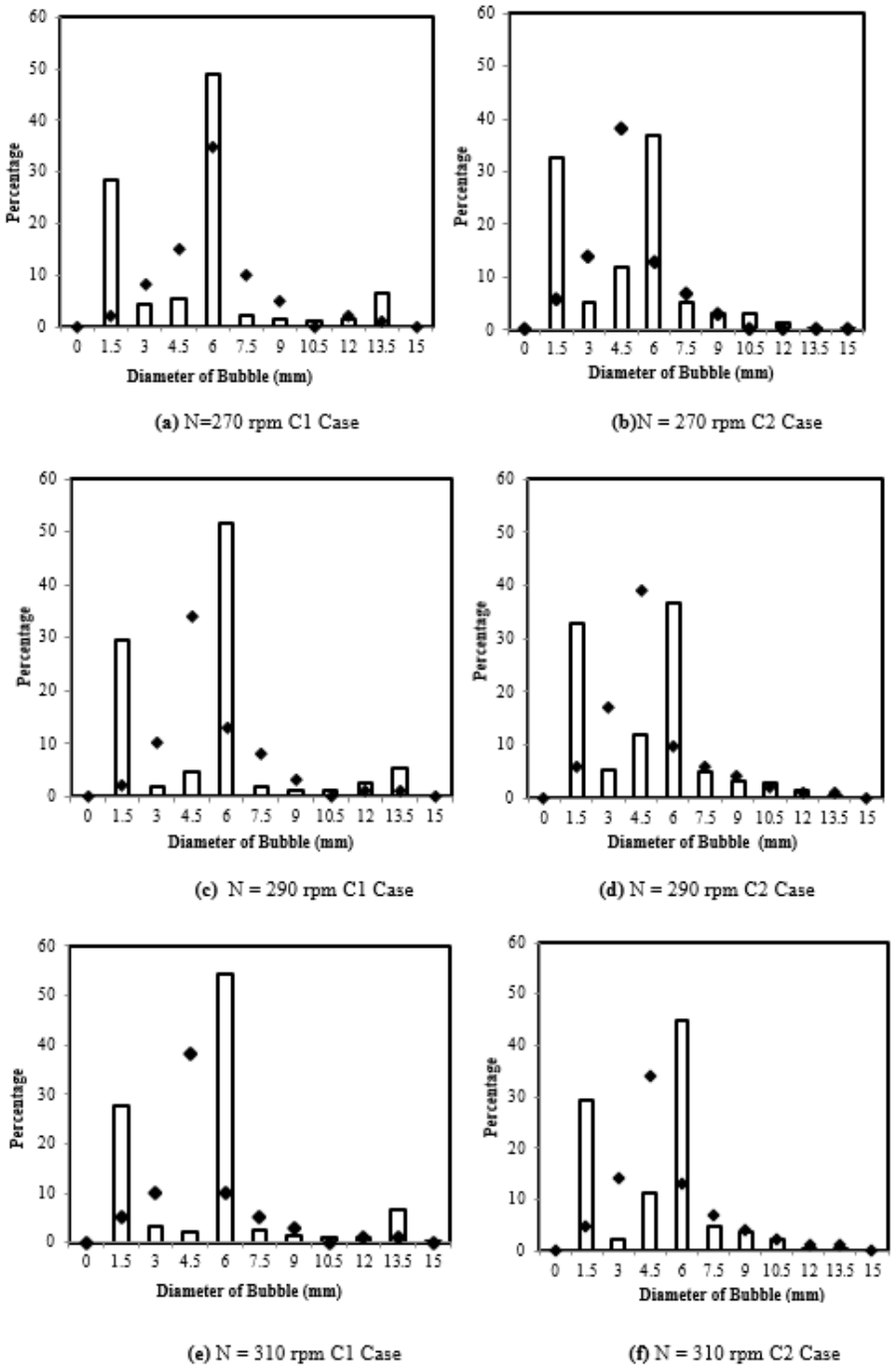

Figure 10. Comparison of air mean bubble diameter for C1 and C2 case for different impeller speed & superficial gas velocity U_G = 0.00094 m/s

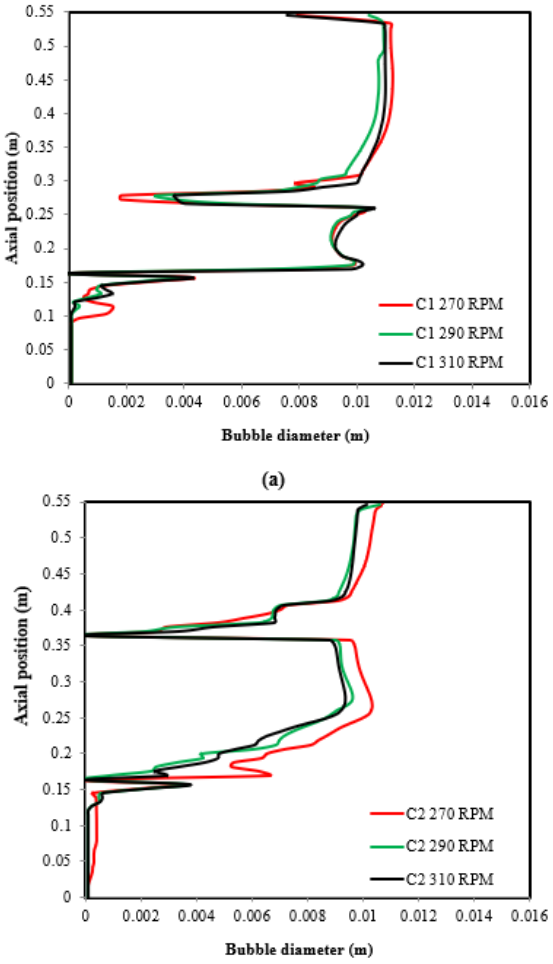

Figure 11. Comparison of bubble diameter on axial position for C1 & C2 impeller configuration for different impeller speeds for U_G = 0.00094 m/s.

From CFD simulation, local bubble size is calculated at axial positions for C1 and C2 impeller configurations at impeller speeds ranging from 270 rpm to 310 rpm at fixed superficial gas velocity U_G = 0.00094 m/s. At axial position 0.25m for C1 case bubble diameter is 0.010252, 0.010078, 0.009905 m while for C2 case 0.010189, 0.009036, 0.008868 m for impeller speed 270, 290, 310 rpm respectively, as shown in Figure11 (a), (b). While at axial position 0.35 m for the C1 case bubble diameter is 0.010715, 0.010617, 0.010198 m while for the C2 case 0.009668, 0.00917, 0.008971 m for 270, 290, 310 rpm respectively. It has been observed from CFD results that the local bubble size for the C2 case is less than the C1 case for fixed operating conditions. Overall, it is observed that the average bubble size for the C2 case is lesser than the C1 Case, and as the rotation speed increases, bubble size decreases for both impeller configurations.

5.3. Effect of impeller configuration on volumetric mass transfer coefficient.

Several different turbulent models are proposed in the literature, and the resulting value of K_La depends largely on which model is used to test data [22]. Experiments were performed for both cases (case C1 and case C2) at different impeller speeds (N) and different gas speeds (U_G). It has been noted that the bubble size is smaller in the C2 case than in the C1 case. There has been a proper distribution throughout the reactor; gas hold-up has also been increased in the C2 case due to this condition. As bubble size decreases, the interfacial area of the bubble increases; due to this, the time spent by the bubble in the stirred tank reactor also increases for

the C2 case. Increased interfacial area resulted in higher mass transfer from the gas phase to the liquid phase. It was also noted that the time for achieving saturation concentration is less for the C2 case than for the C1 case. The volumetric mass transfer coefficient was compared for both configurations, with superficial gas velocity changing from 0.00047 m/s to 0.00141 m/s and impeller rotation speed from 270 rpm to 310 rpm. For the C2 case, which has an impeller clearance of 200 mm, each impeller produces its flow pattern within the stirred tank reactor. CFD simulation results show that for the C2 case, the volume occupied is more, and the volumetric mass transfer coefficient increases with increasing rotation speed and gas flow rate. Figure 12 to Figure 16 depicts the experimental and predicted volumetric mass transfer coefficient for variation in different parameters for C1 and C2. At fixed superficial gas velocity, as the impeller rotation speed increases, the volumetric mass transfer coefficient increases for both C1 and C2 cases for different mass transfer models. Similarly, at a fixed impeller rotation speed, the volumetric mass transfer coefficient increases for both C1 and C2 cases for different mass transfer models as superficial gas velocity increases. It can be seen that from both figures, the experimental volumetric mass transfer coefficient values agree with the slip velocity model. So, for CSTR with sparged gas, the slip velocity mass transfer model is applicable.

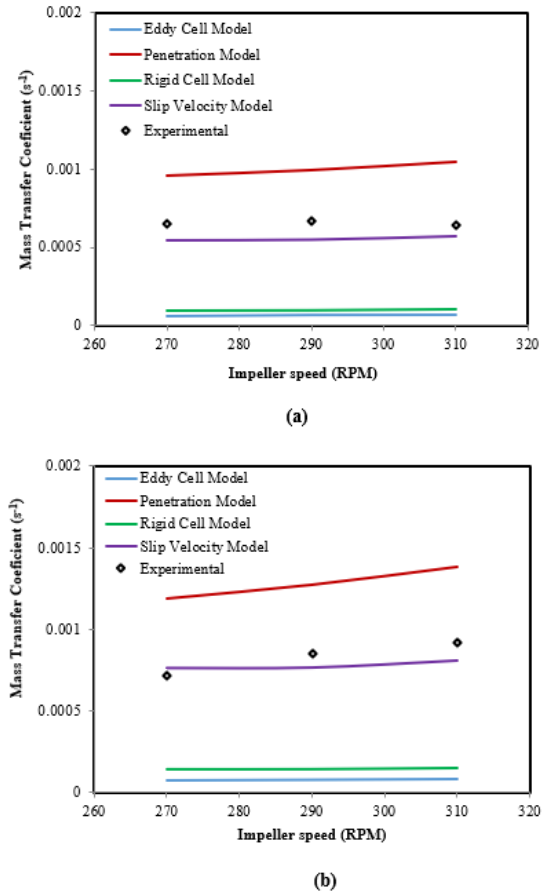

Figure 12. Comparison of experimental and predicted volumetric mass transfer coefficient for different models for (a) C1 &(b) C2 case at different impeller speed & fixed superficial gas velocity 0.0094 m/s.

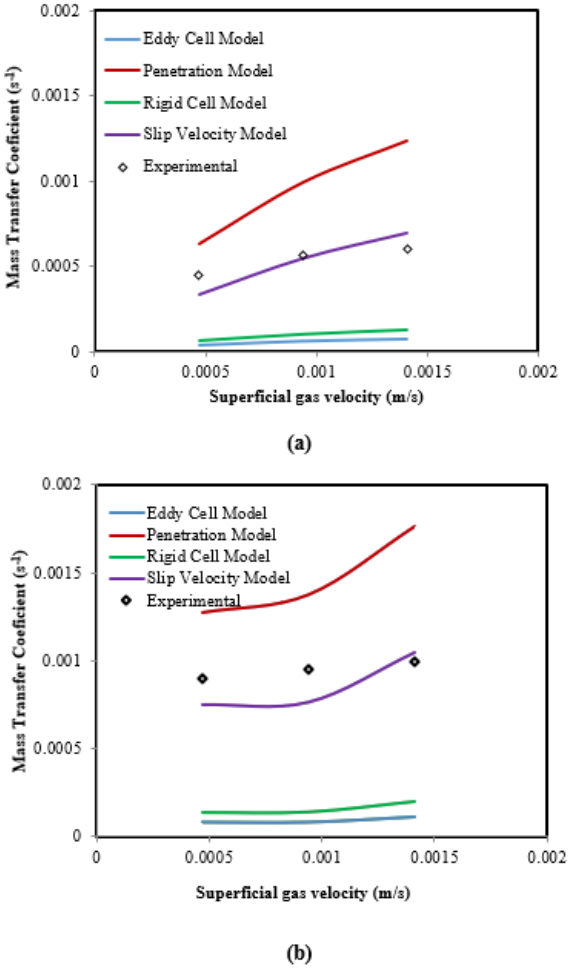

Figure 13. Comparison of experimental and predicted volumetric mass transfer coefficient for different models for (a) C1 & (b) C2 case at different superficial gas velocity& fixed impeller speed 290 rpm.

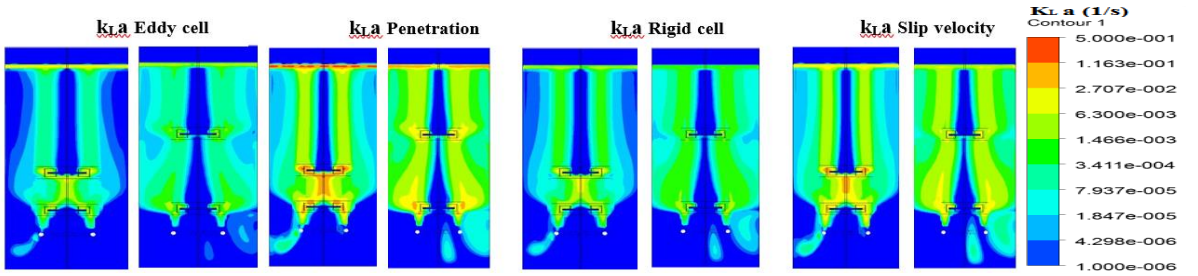

Figure14. Comparison of local volumetric mass transfer coefficient for different models for C1 and C2 case at speed 270 rpm and superficial gas velocity 0.00094 m/s.

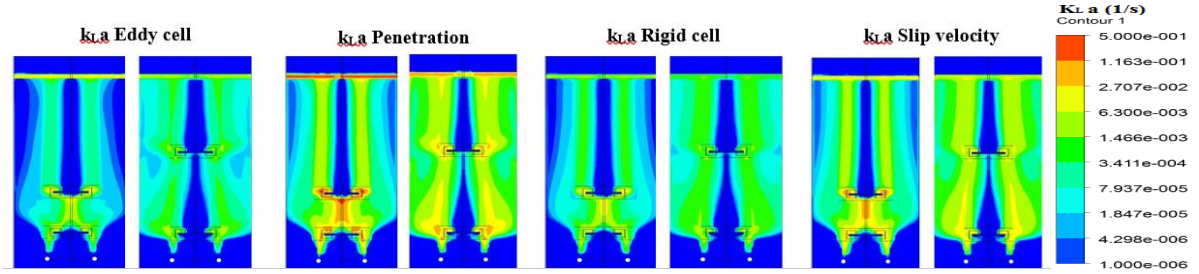

Figure 15. Comparison of local volumetric mass transfer coefficient for different models for C1 and C2 case at speed 290 rpm and superficial gas velocity 0.00094 m/s.

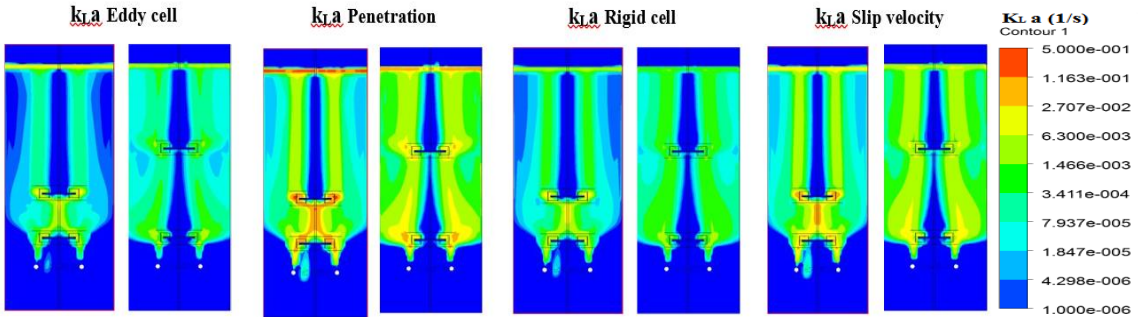

Figure 16. Comparison of local volumetric mass transfer coefficient for different models for C1 and C2 case at speed 310 rpm and superficial gas velocity 0.00094m/s.

5.4. Effect of impeller configuration on power consumption.

Table 5 shows the power consumption for the two-impeller configuration for impeller speed ranging from 270 to 310 rpm and superficial gas velocity ranging from 0.00047 to 0.0014 m/s. As the speed of the impeller increases, so does the power requirement. When gas is introduced into the reactor, the cavities are formed behind impeller blades. With increasing impeller speed, bubble break-up increases, resulting in lower bubble diameter, and large cavities are formed behind impellers. Due to this, the effective density near the impeller blades decreases, causing a reduction in torque value and, ultimately, power consumption. For C1 and C2 impeller configurations, as superficial gas velocity increases from 0.00047 m/s to 0.00094 m/s, the power consumption significantly reduces for fixed impeller speed, as shown in Table 5.

Table 5. Comparison of power consumption for dual impeller configuration for C1 and C2 cases.

Superficial gas velocity (m/s)	Speed of impeller RPM	Power consumption in (W)	
		C1	C2
0.00047	270	1.3	1.41
	290	1.24	1.44
	310	1.10	1.36
0.00094	270	1.76	1.91
	290	1.84	1.91
	310	1.73	1.88

Superficial gas velocity (m/s)	Speed of impeller RPM	Power consumption in (W)	
		C1	C2
0.00141	270	2.49	2.58
	290	2.37	2.40
	310	2.21	2.27

As clearances between impellers were increased to 200 mm from 100 mm, the amount of gas entering the upper impeller lowered than that of Case (C1) as impellers behave as separate entities. The gas entering the upper impeller was less than that of the lower impeller. This ultimately resulted in increased power consumption for Case (C2).

6. Conclusions

The need for better contractors for multiphase systems arose from the realization of sustainable development, where one needs to use the resources carefully and optimize them. The in-depth study of mass transfer coefficient for various systems and contact patterns is important in deciding the type of contactors, contact pattern, and parameter values.

The influence of the distance between impellers in a dual Ruston turbine in a stirred tank reactor determined the stirred tank reactor with dual impeller configuration. Gas hold-up, bubble size distribution, and mass transfer coefficient for dual impeller stirred tank reactor have been determined experimentally. Experimental and predicted gas hold-up and volumetric mass transfer coefficient (K_La) have good agreements with each other for dual impeller configuration of stirred tank reactor. It was observed that the Power consumption for the impeller configuration C2 case was more than the C1 case. The experiment determined bubble size distribution and more bubble break-ups were observed in the C2 case. The experimental study also showed that the volumetric mass transfer coefficient (K_La) improved when the position of the upper impeller was changed to the C2 case. This was because there was adequate breakage of the bubble and increased interfacial area. A computational fluid dynamics (CFD) model was developed to simulate both impeller configurations. The model predicted that the average gas hold-up for the C2 case increased relative to the C1 case. The computational model has qualitatively predicted the identification of the flow regime of upper and lower impeller turbine flooding loading in dual impeller configuration.

Funding

This research received no external funding. All necessary facilities were made available by the Gharda Institute of Technology.

Acknowledgments

The authors are grateful to the Gharda Institute of Technology (GIT) for providing us with the funds to design lab-scale reactors.

Conflict of interest

On behalf of all authors, the corresponding author states that there is no conflict of interest.

References

1. Bouaifi, M.; Roustan, M. Bubble size and mass transfer coefficients in dual-impeller agitated reactors. *Can. J. Chem. Eng.* **1998,** *76*, 390-397, https://doi.org/10.1002/cjce.5450760307.

2. Miller, D.N. Scale-up of agitated vessels gas-liquid mass transfer. *AIChE J.* **1974**, *20*, 445-453, https://doi.org/10.1002/aic.690200303.
3. Machon, V.; Pacek, A.W; Nienow(Fellow), A.W. Bubble Sizes in Electrolyte and Alcohol Solutions in a Turbulent Stirred Vessel. *Chem. Eng. Res. Des.* **1997**, *75*, 339-348, http://doi.org/10.1205/026387697523651.
4. Ford, J.J.; Heindel, T.J.; Jensen, T.C.; Drake, J.B. X-ray computed tomography of a gas-sparged stirred-tank reactor. *Chem. Eng. Sci*. **2008**, *63*, 2075-2085, http://doi.org/10.1016/j.ces.2008.01.007.
5. Shewale, S.D.; Pandit, A.B. Studies in multiple impeller agitated gas-liquid contactors. *Chem. Eng. Sci*. **2006**, *61*, 489-504, http://doi.org/10.1016/j.ces.2005.04.078.
6. Kerdouss, F.; Bannari, A.; Proulx, P. CFD modeling of gas dispersion and bubble size in a double turbine stirred tank. *Chem. Eng. Sci*. **2006**, *61*, 3313-3322, http://doi.org/10.1016/j.ces.2005.11.061.
7. Taghavi, M.; Zadghaffari, R.; Moghaddas, J.; Moghaddas, Y. Experimental and CFD investigation of power consumption in a dual Rushton turbine stirred tank. *Chem. Eng. Res. Des*. **2011**, *89*, 280-290, http://doi.org/10.1016/j.cherd.2010.07.006.
8. Barigou, M.; Greaves, M. Bubble-size distributions in mechanically agitated gas -liquid contactor . *Chem Eng Sci*. **2009**, 47(8), 2009-2025. https://doi.org/10.1016/0009-2509(92)80318-7.
9. Parthasarathy, R.; Ahmed, N. Bubble Size Distribution in a Gas Sparged Vessel Agitated by a Rushton Turbine. *Ind. Eng. Chem. Res*. **1994**, *33*, 703-711, https://doi.org/10.1021/ie00027a032.
10. Bouaifi, M.; Hebrard, G.; Bastoul, D.; Roustan, M. A comparative study of gas hold-up, bubble size, interfacial area and mass transfer coefficients in stirred gas-liquid reactors and bubble columns. *Chem. Eng. Process.* **2001,** *40*, 97-111, https://doi.org/10.1016/S0255-2701(00)00129-X.
11. Teli, S. ; Kulkarni, S. Stirred tank reactor with dual impeller Rushton turbine for application of wastewater treatment - Process optimization and CFD simulation. *Advances in Environmental Technology* 2023, *9*(3), 174-193. https://doi.org/10.22104/aet.2023.6207.1710
12. Moucha, T.; Linek, V.; Prokopová, E. Gas hold-up, mixing time and gas-liquid volumetric mass transfer coefficient of various multiple-impeller configurations: Rushton turbine, pitched blade and techmix impeller and their combinations. *Chem. Eng. Sci*. **2003**, *58*, 1839-1846, http://doi.org/10.1016/S0009-2509(02)00682-6.
13. Mahmoudi, S.M.; Yianneskis, M. The Variation of Flow Pattern and Mixing Time with Impeller Spacing in Stirred Vessels with Two Rushton Impellers. In Fluid Mechanics of Mixing. Fluid Mechanics and Its Applications, King, R., Eds.; Springer, Dordrecht, **1992**, volume 10, 11-18, https://doi.org/10.1007/978-94-015-7973-5_2.
14. Mishra, V.P., Joshi, J.B. LDA Measurements of Flow in Stirred Gas-Liquid Reactors. In Fluid Mechanics of Mixing, Fluid Mechanics and Its Applications, King, R., Eds.; Springer, Dordrecht, **1992**,Volume 10, 217-224, https://doi.org/10.1007/978-94-015-7973-5_25.
15. Komori, S.; Murakami, Y. Turbulent mixing in baffled stirred tanks with vertical-blade impellers. *AIChE J.* **1988**, *34*, 932-937, https://doi.org/10.1002/aic.690340605.
16. Sato, Y.; Sadatomi, M.;Sekoguchi K. Momentum and heat transfer in two-phase bubble flow—I. Theory. *Int. J. Multiph. Flow*. **1981**, *7*, 167-177, https://doi.org/10.1016/0301-9322(81)90003-3.
17. Wodołażski, A. CFD-population balance modelling of catalyst particles in solid-liquid Rushton turbine-agitated tank reactor in scale-up study. *Powder technology* **2017**, *313*, 312-322. https:// doi.org/ 10. 1016/j.powtec.2017.03.03218.
18 Danckwerts, P.V. Significance of Liquid-Flm Coefficients in Gas Absorption. *Indus. Eng. Chem.* **1951**, *43*, 1460–1467, https://doi.org/10.1021/ie50498a055.
19. Frossling, N. Uber die Verdunstung fallenden Tropfen. *Gerlands Beitr. Geophys.* **1938**, *52*, 170-216.
20. Lote, D.A.; Vinod, V.; Patwardhan, A.W. *110th Anniversary:* Numerical Simulations of Gas-Liquid Two-Phase Flow in Vertical Pipe Implementing Population Balance Modeling. *Ind. Eng. Chem. Res*. **2019**, *58*, 8437-8455, https://doi.org/10.1021/acs.iecr.9b00912.
21. Hudcova, V.; Machon, V.; Nienow, A. W. (Gas–liquid dispersion with dual Rushton impellers. *Biotechnology and Bioengineering* **1989**, *34*(5), 617-628. https://doi.org/10.1002/bit.260340506
22. Forrester, S.E.; Rielly, C.D.; Carpenter, K.J. Gas-inducing impeller design and performance characteristics. *Chem. Eng. Sci*. **1998**, *53*, 603-615, https://doi.org/10.1016/S0009-2509(97)00352-7.
23. Luo, H.; Wang, X.; Liu, X.; Wu, X.; Shi, X.; Xiong, Q. A review on CFD simulation of biomass pyrolysis in fluidized bed reactors with emphasis on particle-scale models. *J. Anal. Appl. Pyrolysis* **2022**, *162*, 105433, https://doi.org/10.1016/j.jaap.2022.105433.

24. Thakur, A.K.; Kumar, R.; Banerjee, N.; Chaudhari, P.; Gaurav, G.K. Hydrodynamic modeling of liquid-solid flow in polyolefin slurry reactors using CFD techniques–A critical analysis. *Powder Technol.* **2022**, *405*, 117544, https://doi.org/10.1016/j.powtec.2022.117544.
25. de Brito Lira, J.O.; Riella, H.G.; Padoin, N.; Soares, C. Fluid dynamics and mass transfer in curved reactors: A CFD study on Dean flow effects. *J. Environ. Chem. Eng.* **2022**, *10*, 108304, https://doi.org/10.1016/j.jece.2022.108304.
26. Bouras, H.; Haroun, Y.; Bodziony, F.F.; Philippe, R.; Fongarland, P.; Augier, F. Use of CFD for pressure drop, liquid saturation and wetting predictions in trickle bed reactors for different catalyst particle shapes. *Chemical Engineering Science*. **2022**, 249, 117315. https://doi.org/10.1016/j.ces.2021.117315.
27. Abdel-Gawad, E.H.; Taha, M.M.; Abdel-Kawi, M.A.; Sedahmed, G.H.; El-Naggar, M.A. Mass and heat transfer in stirred tank equipped with a horizontal tubular cruciform baffle. *Chem. Eng. Res. Design*. **2022**, *178*, 514-522, https://doi.org/10.1016/j.cherd.2021.12.045.
28. Xu, X.; Wang, L.; Wang, H.; Liu, H.; Yang, Q. Circulating jet for enhancing the mass transfer in a gas–liquid stirred tank reactor. *AIChE J.* **2022,** *68*, e17392, https://doi.org/10.1002/aic.17392.
29. Fathalla, A.S.; Amin, N.K.; El-Ashtoukhy, E.S.Z.; Sedahmed, G.H. Heat and Mass Transfer at the Wall of a Square Mechanically Stirred Gas-Liquid-Solid Catalytic Reactor. *Chem. Eng. Technol.* **2022**, *45*, 58-66, https://doi.org/10.1002/ceat.202100142.
30. Miao, E.; Zheng, X.; Xiong, Z.; Zhao, Y.; Zhang, J. Kinetic modeling of direct aqueous mineral carbonation using carbide slag in a stirred tank reactor. *Fuel* **2022,** *315*, 122837, https://doi.org/10.1016/j.fuel.2021.122837.
31. Jadhav, A.J.; Barigou, M. Eulerian-Lagrangian Modelling of Turbulent Two-Phase Particle-Liquid Flow in a Stirred Vessel: CFD and Experiments Compared. *Int. J. Multiph. Flow.* **2022**, *155*, 104191, https://doi.org/10.1016/j.ijmultiphaseflow.2022.104191.
32. Kahouadji, L.; Liang, F.; Valdes, J.P.; Shin, S.; Chergui, J.; Juric, D.; Craster, R.V.; Matar, O.K. The transition to aeration in turbulent two-phase mixing in stirred vessels. *Flow* **2022**, *2*, E30, https://doi.org/10.1017/flo.2022.24.
33. Maluta, F.; Paglianti, A.; Montante, G. Towards a CFD-PBE simulation of aerated stirred tanks at high gas hold ups and different flow regimes. *Chem. Eng. Res. Design* **2022**, *180*, 425-436, https://doi.org/10.1016/j.cherd.2021.10.018.
34. Li, S.; Yang, R.; Wang, C.; Han, H.; Shen, S.; Wang, H. CFD–PBM Simulation on Bubble Size Distribution in a Gas–Liquid–Solid Flow Three-Phase Flow Stirred Tank. *ACS Omega* **2022**, *7*, 1934-1942, https://doi.org/10.1021/acsomega.1c05406.
35. Sheikh, H.A.; Savari C.; Barigou M. A data-driven stochastic model for velocity field and phase distribution in stirred particle-liquid suspensions. *Powder Technol.* **2022**, *411*, 117940, https://doi.org/10.1016/j.powtec.2022.117940.
36. Ryashko, L.; Bashkirtseva, I. Stochastic Bifurcations and Excitement in the ZS-Model of a Thermochemical Reaction. *Mathematics* **2022**, *10*, 960, https://doi.org/10.3390/math10060960.
37. Kishida, M.; Ogura M. Temporal deep unfolding for constrained nonlinear stochastic optimal control. *IET Control. Theory Appl.* **2022**, *16*,139-150, https://doi.org/10.1049/cth2.12207.
38. Alsadiq, Y.A. Best Performance of Reactor Controllers Using Stochastic Optimization Method. *Sirte University Scientific Journal*. **2022,** *12*,16-37.
39. Wu, Q.; Zhang, G.; Wang, B.; Zhong, L.; Xiao, F. Performance Comparison of Deterministic and Stochastic Modifications in Stokes's and Hotine's Formulas: The Case of Jilin Province, China. *Remote Sens.* **2023**, *15*, 376, https://doi.org/10.3390/rs15020376.
40. Röhl, S.; Hohl, L.; Stock, S.; Zhan, M.; Kopf, T.; von Klitzing, R.; Kraume, M. Application of Population Balance Models in Particle-Stabilized Dispersions. *Nanomaterials* **2023**, *13*, 698, https://doi.org/10.3390/nano13040698.
41. Tang, H.; Fan, Y.; Ma, X.; Dong, X.; Chang, M.; Li, N. Modelling Flocculation in a Thickener Feedwell Using a Coupled Computational Fluid Dynamics–Population Balance Model. *Minerals* **2023**, *13*, 309, https://doi.org/10.3390/min13030309.